

Ultra Low Power Bioelectronics

Fundamentals, Biomedical Applications,
and Bio-inspired Systems

Chapter 24

RAHUL SARPESHKAR

Massachusetts Institute of Technology



CAMBRIDGE
UNIVERSITY PRESS

Copyright 2010

24 Cytomorphic electronics: cell-inspired electronics for systems and synthetic biology

Any living cell carries with it the experience of a billion years of experimentation by its ancestors.

Max Delbrück

The cells in the human body provide examples of phenomenally energy-efficient sensing, actuation, and processing. An average $\sim 10\ \mu\text{m}$ -size human cell hydrolyzes several energy-carrying adenosine-tri-phosphate (ATP) molecules within it to perform nearly $\sim 10^7$ ATP-dependent biochemical operations per second [1]. Since, under the conditions in the body, the hydrolysis of each ATP molecule provides about $20\ \text{kT}$ ($8 \times 10^{-20}\ \text{J}$) of metabolic energy, the net power consumption of a single human cell is an astoundingly low $0.8\ \text{pW}$! The ~ 100 trillion cells of the human body thus have an average resting power consumption of $\sim 80\ \text{W}$, consistent with numbers derived from the Appendix of Chapter 23.

The cell processes its mechanical and chemical input signals with highly noisy and imprecise parts. Nevertheless, it performs complex, highly sensitive, and collectively precise hybrid analog-digital signal processing on its inputs such that reliable outputs are produced. Such signal processing enables the cell to sense and amplify minute changes in the concentrations of specific molecules amidst a background of confoundingly similar molecules, to harvest and metabolize energy contained in molecules in its environment, to detoxify and/or transport poisonous molecules out of it, to sense if it has been infected by a virus, to communicate with other cells in its neighborhood, to move, to maintain its structure, to regulate its growth in response to signals in its surround, to speed up chemical reactions via sophisticated enzymes, and to replicate itself when it is appropriate to do so. The $\sim 30,000$ -node gene-protein and protein-protein molecular interaction networks within a cell that implement and regulate these functions are a true marvel of nanotechnology. The nanotechnology of man appears crude and primitive when contrasted with that in nature's cells.

In this chapter, we show that the equations that describe subthreshold transistor operation and the equations that describe chemical reactions have strikingly detailed similarity, including stochastic properties. Therefore, any chemical reaction can be efficiently and programmably represented with a handful of subthreshold (or bipolar) transistors that comprise an analog circuit. Intracellular protein-protein biochemical reaction networks can then potentially be modeled by

hooking such circuits to each other. DNA-protein networks can also be efficiently modeled with such analog circuits. DNA-protein networks can be modeled even more efficiently with hybrid analog-digital circuits that approximate nonlinear analog characteristics with more approximate digital ones. Since extracellular cell-cell networks also rely on molecular binding and chemical reactions, networks such as hormonal networks or neuronal networks can also be efficiently modeled. Thus, in the future, we can potentially attempt to simulate cells, organs, and tissues with ultra-fast highly parallel analog and hybrid analog-digital circuits including molecular stochastics and cell-to-cell variability on large-scale electronic chips. Such molecular-dynamics simulations are extremely computationally intensive especially when the effects of noise, nonlinearity, network-feedback effects, and cell-to-cell variability are included. Stochastics and cell-to-cell variability are highly important factors for predicting a cell's response to drug treatment, e.g., the response of tumor cells to chemotherapy treatments [2]. We will show in this chapter that circuit, feedback, and noise-analysis techniques described in the rest of this book can shed insight into the systems biology of the cell [3]. For example, flux balance analysis is frequently used to reduce the search space of parameters in a cell [4]. It is automatically implemented as Kirchhoff's current law in circuits since molecular fluxes map to circuit currents. Similarly, Kirchhoff's voltage law automatically implements the laws of thermodynamic energy balance in chemical-reaction loops. We shall provide other examples throughout the chapter. An excellent introduction to systems biology may be found in [5]. Robustness analysis of the circuit using return-ratio techniques can shed insight in the future into which genes, when mutated, will lead to disease in a network, and which will not. Circuit-design techniques can also be mapped to create synthetic-biology circuits that perform useful functions in the future [6].

Circuits in biology and circuits in electronics may be viewed as being highly similar with biology using molecules, ions, proteins, and DNA rather than electrons and transistors. Just as neural circuits have led to biologically inspired neuromorphic electronics, cellular circuits can lead to a novel biologically inspired field that we introduce in this chapter and term *cytomorphic electronics*. In fact, we will show that there are many similarities between spiking-neuron computation and cellular computation. The hybrid state machines (HSMs) described in Chapters 22 and 23 (see Figure 22.9 (b)) provide a useful framework for thinking about cellular circuits with active DNA genes in the cell being represented by digital variables and protein concentrations represented by analog variables. DNA-protein interactions are represented by interactions between the analog and digital parts of an HSM. Networks of hybrid state machines can model networks of cells. The ZY transmission-line architectures that we discussed in Chapter 23 for describing computation in the retina, the cochlea, the vocal tract, and neuronal dendrites are also useful for understanding nonlinear reaction-diffusion partial differential equations in cells. Ingenious nonlinear transmission lines are exploited by the cell to create spatially decaying molecular-concentration profiles that are robustly invariant to changes in protein-production rates during development.

Leonardo da Vinci, perhaps the first bio-inspired engineer in mankind, said: ‘Human subtlety will never devise an invention more beautiful, more simple or more direct than does nature because in her inventions nothing is lacking, and nothing is superfluous.’ One is indeed awed and humbled as one learns more and more about the ingenious operation of even a single cell. We have much to learn from nature in architecting clever electronics, algorithms, and nanostructures. This chapter will only attempt to scratch the surface.

24.1 Electronic analogies of chemical reactions

Figure 24.1 illustrates that there are striking similarities between chemical reaction dynamics (Figure 24.1 (a)) and electronic current flow in the subthreshold regime of transistor operation (Figure 24.1 (b)): electron concentration at the source is analogous to reactant concentration; electron concentration at the drain is analogous to product concentration; forward and reverse current flows in the transistor are analogous to forward and reverse reaction rates in a chemical reaction; the forward and reverse currents in a transistor are exponential in voltage differences at its terminals analogous to reaction rates being exponential in the free energy differences in a chemical reaction; increases in gate voltage lower energy barriers in a transistor increasing current flow analogous to the effects of enzymes or catalysts in chemical reactions that increase reaction rates; and the stochastic Poisson shot noise in subthreshold transistors are analogous to the stochastic molecular shot noise in reactions. These analogies suggest that one can mimic and model large-scale chemical-processing systems in biological and artificial networks very efficiently on an electronic chip at time scales that could be a million to billion times faster. No one, thus far, appears to have exploited the detailed similarity behind the equations of chemistry and the equations of electronics to build such networks. The single-transistor analogy of Figure 24.1 is already an exact representation of the chemical reaction $A \rightleftharpoons B$ including

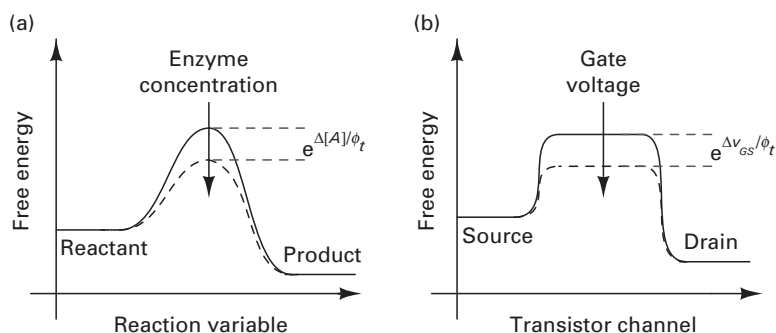


Figure 24.1a, b. Similarities between chemical reaction dynamics (a) and subthreshold transistor electronic flow (b). Reprinted with permission from [9] (©2009 IEEE).

stochastics, with forward electron flow from source to drain corresponding to the $A \rightarrow B$ molecular flow and backward electron flow from drain to source corresponding to the $B \rightarrow A$ molecular flow. In this chapter, we shall build on the key idea of Figure 24.1 to show how to create current-mode subthreshold transistor circuits for modeling arbitrary chemical reactions. We can then create large-scale biochemical reaction networks from such circuits for modeling computation within and amongst cells. Before we do so, we provide another example of a voltage-mode resistor circuit that can efficiently represent the differential equations that describe association and dissociation chemical reactions.

An association chemical reaction, for example, that between an enzyme E and a substrate S , is described by



In Equation (24.1), the enzyme binds to the substrate to create a bound enzyme ES or E_b via a forward reaction with reaction-rate constant k_f . The product E_b also dissociates via a backward reaction with reaction-rate constant k_r to recreate E and S . The total amount of enzyme $E_t = E + E_b$ is a constant invariant with time and composed of enzyme in free (E) or bound (E_b) form. If the concentrations of each variable are denoted by square brackets around the variable and the substrate concentration is assumed constant at $[S]$, the equations that describe the mass-action kinetics of the chemical reaction are given by

$$\begin{aligned} \frac{d[E_b]}{dt} &= k_f[E][S] - k_r[E_b] \\ [E] &= [E_t] - [E_b] \end{aligned} \quad (24.2)$$

If $C = 1$, the equations of Equation (24.2) are represented by the resistive-divider circuit of Figure 24.2 (a) with resistances of value $1/(k_f[S])$ and $1/k_r$; the currents through these resistances represent the forward and backward fluxes of the chemical reaction in the first line of Equation (24.2). At equilibrium, when the capacitor voltage has reached a constant value, these two currents are equal and the circuit functions like a resistive divider. From simple resistive-divider analysis, some algebra reveals that, under these conditions,

$$\begin{aligned} [E_b] &= [E_t] \left(\frac{[S]/K_d}{([S]/K_d) + 1} \right) \\ K_d &= \frac{k_r}{k_f} \\ K_{eq} &= \frac{k_f}{k_r} = \frac{1}{K_d} \end{aligned} \quad (24.3)$$

Thus, when $[S]$ is significantly greater than K_d , the enzyme substrate binding is said to exhibit saturation, since the fraction of bound enzyme is limited by the total enzyme concentration $[E_t]$ rather than by the substrate concentration $[S]$. The circuit of Figure 24.2 (a) reveals that circuit analogies allow us to rapidly

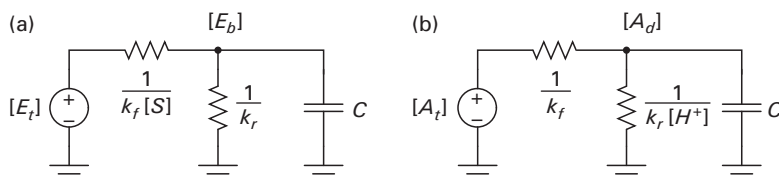


Figure 24.2a, b. Michaelis-Menten association reaction and acid dissociation reaction.

understand Michaelis-Menten kinetics of enzyme-substrate saturation or of another association reaction as resistive-divider saturation.

In many biological systems, typically $[E_b]$ leads to significantly slower production of a product P at a flux rate of $v[E_b]$ via a further unidirectional reaction, accompanied by unbinding of the enzyme and substrate. This reaction is easily represented by including a resistance of value $1/v$ in parallel with the resistance $1/k_r$ in Figure 24.2 (a); in addition, a voltage-dependent transconductance whose output current depends on $[E_b]$ as $v[E_b]$ charges a capacitance $C_2 = 1$; the capacitor's voltage then represents the concentration of P . Thus, simple circuit blocks can also represent Michaelis-Menten kinetics more exactly if needed. However, the essential dynamics of Michaelis-Menten kinetics are well represented by Equations (24.2), (24.3), and Figure 24.2 (a).

A dissociation reaction, e.g., that due to an acid, is given by



The reader should be able to show that the circuit of Figure 24.2 (b) represents this reaction with $[A_t]$ being the amount of acid in total form (undissociated as HA) or dissociated as $[A^-] = [A_d]$, i.e., $[A_t] = [HA] + [A_d]$.

Every chemical reaction, e.g., the enzyme-substrate binding illustrated in Figure 24.3, implicitly has two negative-feedback loops embedded within it. The first feedback loop arises because the concentration of reactants falls if the concentration of products builds, thus slowing the forward reaction; this constitutes the major loop of Figure 24.3. The second feedback loop arises because the backward reaction speeds up when the concentration of products builds; this constitutes the minor loop in Figure 24.3. At steady state, the $1/s$ integrator has infinite gain such that the feedback path of the minor loop determines the closed-loop transfer function of the minor loop. Thus, the feedback loop of Figure 24.3 also leads to Michaelis-Menten saturation except that the saturation is now viewed as a high-loop-gain effect with loop gain $[S]/K_d$. The major loop in Figure 24.3 corresponds to the restorative current through resistance $1/k_f$ in Figure 24.2 (a). The minor loop in Figure 24.3 corresponds to the restorative current through $1/k_r$ in Figure 24.2 (a).

One difference between the chemical resistive-divider circuit of Figure 24.2 (a) and actual electronic resistive-divider circuits lies in their noise properties. The current in real resistors flows by drift while their $4kTR$ current noise per unit

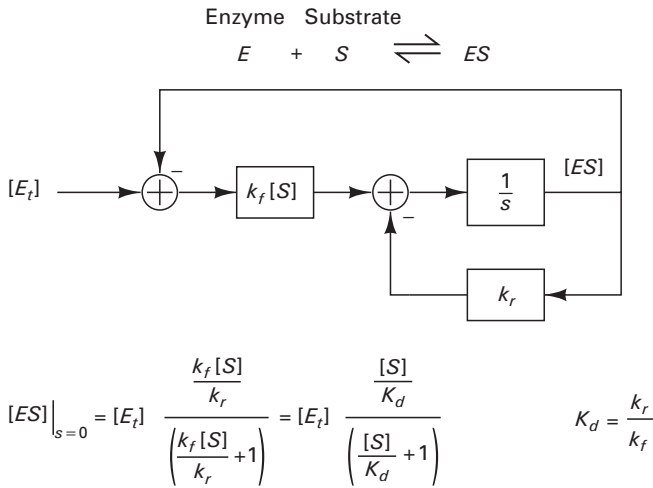


Figure 24.3. The two feedback loops embedded in any chemical reaction.

bandwidth is due to the shot noise of internal diffusion currents (see Chapter 7 on noise). In contrast, in Figure 24.2 (a), the resistor current *and* resistor noise currents are both due to diffusion currents that exhibit Poisson noise statistics. Thus, in Figure 24.2 (a) the resistor's noise is simply the shot noise of the current flowing through it and varies as the current through the resistor varies. Hence, the subthreshold transistor analogy of Figure 24.1 is more accurate than that of the resistor analogy of Figure 24.2 (a) since it gets both the current and the noise exactly correct (for the $A \rightleftharpoons B$ reaction). Nevertheless, if we use the correct shot-noise formulas that pertain to the resistors of Figure 24.2 (a), we can still exploit the techniques of Chapters 7 and 8 to compute the total concentration noise $\overline{v_n^2}$ on the capacitor C : the shot noise of the currents flowing through the $1/(k_f[S])$ and $1/(k_r)$ resistors is converted to voltage noise on the capacitor C as in a simple RC circuit with two resistors in parallel. Since we are interested in mass currents rather than charge currents, we set

$$\begin{aligned} q &= 1 \\ C &= \text{Volume} \end{aligned} \quad (24.5)$$

If we assume that $[S]$ is nearly constant and exhibits no noise, for example, because $[S]$ is large, we get

$$\begin{aligned} k'_f &= k_f[S] \\ \overline{v_n^2} &= 2q \left(E_t \left(1 - \frac{k'_f}{k'_f + k_r} \right) k'_f + E_t \left(\frac{k'_f}{k'_f + k_r} \right) k_r \right) \times \frac{1}{(k'_f + k_r)^2} \times \frac{k'_f + k_r}{2\pi C} \times \frac{\pi}{2} \\ \overline{v_n^2} &= 4qE_t \left(\frac{k'_f k_r}{k'_f + k_r} \right) \frac{1}{(k'_f + k_r)} \times \frac{1}{4C} \end{aligned}$$

$$\begin{aligned}
 &= \frac{E_t}{C} \frac{k'_f k_r}{(k'_f + k_r)^2} \\
 \overline{v_n^2} &= \frac{E_t}{C} \left(\frac{k'_f}{k'_f + k_r} \right) \left(\frac{k_r}{k'_f + k_r} \right)
 \end{aligned} \tag{24.6}$$

The result of Equation (24.6) has the $1/C$ scaling expected from the usual kT/C relationship for the noise on a capacitor. If we compute the total fluctuation in the number of bound enzyme molecules, σ_N , on the capacitor C (i.e., the chemical analog of the charge fluctuation on capacitor C rather than the voltage fluctuation), we get

$$\begin{aligned}
 \sqrt{\sigma_N^2} &= \left(\sqrt{\frac{E_t}{C} \left(\frac{k'_f}{k'_f + k_r} \right) \left(\frac{k_r}{k'_f + k_r} \right)} \right) C \\
 \sigma_N &= \left(\sqrt{E_t C \left(\frac{k'_f}{k'_f + k_r} \right) \left(\frac{k_r}{k'_f + k_r} \right)} \right) \\
 \sigma_N &= \sqrt{N_t p(1-p)}
 \end{aligned} \tag{24.7}$$

where $N_t = E_t C$ is the total number of enzyme molecules within the volume compartment C of the reaction, whether bound or unbound, and p is the probability that an enzyme molecule is bound. Thus, we find that the noise is maximized when the probability of an enzyme molecule being bound is $1/2$ and minimized when it is near 1 or 0. Intuitively, a chemical reaction that has a forward flux greatly in excess of the reverse flux ($p = 1$) or vice versa ($p = 0$) will exhibit little noise since almost all molecules will be bound or unbound respectively. Similarly, a transport channel in a cell membrane exhibits the least noise when the probability for its opening is near 1 or 0 [7].

24.2 Log-domain current-mode models of chemical reactions and protein-protein networks

The dynamics of a chemical species i with concentration x_i in a chemical reaction can be described by a differential equation of the form

$$\frac{dx_i}{dt} = \sum_j c_j + \sum_l k_{il} u_l + \sum_m k_{im} x_m + \sum_{lm} k_{ilm} x_l x_m + \sum_{np} k_{inp} x_n u_p + \dots \tag{24.8}$$

where various externally controlled input species $u(t)$ and state-variable chemical species $x(t)$ interact via zeroth order (the c_j terms), first order (the k_{il} and k_{im} terms), second order (the k_{ilm} and k_{inp} terms), or higher-order interactions

to create fluxes that increase x_i (positive kinetic rate constants k) or decrease x_i (negative kinetic rate constants k). In almost all chemical reactions, reaction mechanisms at practical temperatures, pressures, and concentrations are such that only terms up to second order in Equation (24.8) are sufficient for describing the dynamics of all species that are involved. Higher-order terms due to the simultaneous association or dissociation of more than two chemical species have vanishingly low probability: most reactions that involve the association or dissociation of more than two species usually occur via chemical intermediates with at most two species associating or dissociating at any given time. Thus, truncating Equation (24.8) after the second-order terms is usually an excellent description of chemical dynamics for all species. Note that an equation such as Equation (24.8) must be written for every state-variable species i involved in the reaction. Furthermore, the outputs $y_i(t)$ can be a linear combination of the input species

$$y_i = \sum_j r_{ij}x_j + \sum_j s_{ij}u_j \quad (24.9)$$

Thus, chemical reaction dynamics are typically described by polynomially nonlinear differential equations with an order of two. Linear systems are an example of polynomial differential equations with an order of one. Note that we have assumed mass-action kinetics and a well-mixed spatially homogeneous medium in formulating Equation (24.8).

We know from Chapter 14 on current-mode circuits that translinear circuits are capable of creating static nonlinear systems and linear dynamical systems through the use of exponential nonlinear devices. Given the similarities between chemical computation and electronic computation illustrated in Figure 24.1, both of which involve exponential nonlinearities, we may wonder if log-domain bipolar and subthreshold circuits with exponential nonlinearities can mimic the dynamics of chemical reaction networks. We now show that it is indeed possible to do so, in fact, for polynomially nonlinear dynamical systems of any order. For the most part, we shall focus on second-order systems only since they are most relevant for modeling chemical reactions within cells.

To map chemical reaction networks to current-mode circuits, we must have an appropriate amplitude and time-constant scaling from the chemical to the electrical domain. Amplitude scaling is easily accomplished by setting

$$\frac{x_i}{X_0} = \frac{i_i}{I_0} \quad (24.10)$$

Equation (24.10) states that the normalized concentration of the chemical concentration x_i with respect to a global reference concentration, X_0 , is equal to the normalized current, i_i , with respect to a global reference current I_0 . To make the normalized electrical state variable i_i/I_0 have a time derivative that is α times faster than the normalized chemical state variable x_i/X_0 , the kinetic rate constants in the chemical equation need to be replaced by equivalent electrical

rate constants. Thus, a kinetic term in a chemical differential equation will scale according to

$$\begin{aligned}
 \frac{dx_i}{dt} &= \dots + \sum_{lm} k_{ilm} x_l x_m + \dots \\
 X_0 \frac{d(x_i/X_0)}{dt} &= \dots + X_0^2 \sum_{lm} k_{ilm} \frac{x_l}{X_0} \frac{x_m}{X_0} + \dots \\
 X_0 \left(\frac{1}{\alpha} \right) \frac{d(i_i/I_0)}{dt} &= \dots + X_0^2 \sum_{lm} k_{ilm} \frac{i_l}{I_0} \frac{i_m}{I_0} + \dots \\
 \frac{d(i_i/I_0)}{dt} &= \dots + \sum_{lm} (\alpha X_0^1 k_{ilm}) \frac{i_l}{I_0} \frac{i_m}{I_0} + \dots
 \end{aligned} \tag{24.11}$$

That is a kinetic rate constant transforms according to

$$k \rightarrow \alpha X_0^{(S-1)} k \tag{24.12}$$

when we map from the chemical domain to the electrical domain; here, S is the order of the term in the chemical equation (zeroth, first-order, second-order, ...). Note that input u terms in the chemical equation are also normalized by X_0 , so the scaling of Equation (24.12) also applies to them.

The last row of Equation (24.11) can be transformed into a form suitable for a log-domain dynamical system, if we multiply the left hand and right hand sides by the reciprocal of i_i/I_0 (see Chapter 14), perform some further multiplications on both sides, and do some algebra:

$$\begin{aligned}
 \frac{1}{(i_i/I_0)} \frac{d(i_i/I_0)}{dt} &= \dots + \sum_{lm} (\alpha X_0^1 k_{ilm}) \frac{\frac{i_l}{I_0} \frac{i_m}{I_0}}{(i_i/I_0)} + \dots \\
 \frac{C_i \frac{\phi_i}{\kappa} di_i}{i_i dt} &= \dots + I_0 \sum_{lm} \left(\alpha \frac{C_i \frac{\phi_i}{\kappa}}{I_0} X_0^1 k_{ilm} \right) \frac{\frac{i_l}{I_0} \frac{i_m}{I_0}}{(i_i/I_0)} + \dots \\
 C_i \frac{dv_{Ci}}{dt} &= \dots + I_0 \sum_{lm} (\beta_{ilm}) \frac{\frac{i_l}{I_0} \frac{i_m}{I_0}}{(i_i/I_0)} + \dots \\
 \beta_{ilm} &= \alpha \frac{C_i \frac{\phi_i}{\kappa}}{I_0} X_0^1 k_{ilm} \\
 \beta_{ilm} &= \alpha \tau_{0i} X_0^1 k_{ilm}
 \end{aligned} \tag{24.13}$$

where v_{Ci} is the log-domain voltage on capacitor C_i that represents $\log(x_i/X_0)$ as $(\phi_i/\kappa)\ln(i_i/I_0)$ with (ϕ_i/κ) being the characteristic subthreshold exponential voltage ($\kappa = 1$ in the case of a bipolar), and $\tau_{0i} = C_i(\phi_i/\kappa)/I_0$ being a characteristic electrical time constant. All terms undergo similar transformation like the second-order term in Equation (24.13): that is, Equation (24.8) is described by the following transformation

$$\begin{aligned}
 \frac{dx_i}{dt} &= \dots + \sum_m k_{im} x_m + \sum_{lm} k_{ilm} x_l x_m + \sum_{np} k_{inp} x_n u_p + \dots \\
 C_i \frac{dv_{Ci}}{dt} &= I_0 \left(\dots + \sum_m \beta_{im} \frac{i_m/I_0}{i_i/I_0} + \sum_{lm} \beta_{ilm} \frac{(i_l/I_0)(i_m/I_0)}{i_i/I_0} + \sum_{np} \beta_{inp} \frac{(i_n/I_0)(u_p/I_0)}{i_i/I_0} + \dots \right)
 \end{aligned} \tag{24.14}$$

where the dimensionless β_i kinetic rate constants in the electrical system are related to their corresponding chemical ones according to

$$\beta_{i..} = (\alpha\tau_{0i}X_0^{S-1})k_i \quad (24.15)$$

where $S = [0, 1, 2]$ depending on whether the term is zeroth, first, or second order. Note that Equations (24.14) and (24.15) describe transformations for a particular chemical species i but an identical transformation applies to all other species involved in the dynamics with one capacitor C_i per state variable x_i . That is, if the original chemical dynamical system had N state variables, M inputs, and P outputs, the transformed electrical dynamical system will have N capacitors, M current inputs, and P current outputs. More formally, consider a reaction system consisting of N species \mathbf{x} , M inputs \mathbf{u} , and P outputs \mathbf{y} . If we assume zeroth, first, and second order mass-action kinetics only, and model forward and backward reactions through separate unidirectional differential equations, we may describe such a system by

$$\begin{aligned} \frac{d\mathbf{x}}{dt} &= \mathbf{C} + \mathbf{D}\mathbf{x} + \mathbf{E}(\mathbf{x} \otimes \mathbf{x}) + \mathbf{F}\mathbf{u} + \mathbf{G}(\mathbf{x} \otimes \mathbf{u}) \\ \mathbf{y} &= \mathbf{H}\mathbf{x} + \mathbf{K}\mathbf{u} \end{aligned} \quad (24.16)$$

where \otimes is the outer product of two vectors. The similarity of Equation (24.16) to the standard state-space equations of linear control theory should be evident [8]. The $(\mathbf{x} \otimes \mathbf{x})$ terms add polynomial nonlinearities of order 2 such that Equation (24.16) differs from the standard linear equations of control theory.

As an example, to implement the differential equations that model the second-order unidirectional association reaction $A + B \rightarrow C$, the current-mode integrator of Chapter 14 is modified to create the log-domain circuit of Figure 24.4. This circuit implements the differential equations

$$\begin{aligned} \beta &= \beta_1\beta_2 \\ C \frac{dv_C}{dt} &= -\beta \frac{i_A i_B}{i_C} \\ C \frac{dv_B}{dt} &= +\beta \frac{i_A i_B}{i_B} = +\beta i_A \\ C \frac{dv_A}{dt} &= +\beta \frac{i_A i_B}{i_A} = +\beta i_B \end{aligned} \quad (24.17)$$

Note that the signs of the currents have been reversed because the state variable v_i in Figure 24.4 is referenced to V_{DD} , i.e., given by $V_{DD} - v_i$. The parameters β_1 and β_2 are altered via DAC-programmable bias currents with $\beta = \beta_1\beta_2$; thus, a large dynamic range of programmability in β is achieved with two lower dynamic range DACs.

In Figure 24.4, we can keep the concentrations of i_A constant and i_B constant (hold the voltage of nodes v_A and v_B) and implement the backward reaction ($C \rightarrow A + B$) via a similar circuit and then vary $K_d = I_0\beta_r/\beta_f$ by varying the backward-reaction β_r compared with the forward-reaction β_f . In normal non-log-voltage units, the overall current-mode circuit then simulates a constant

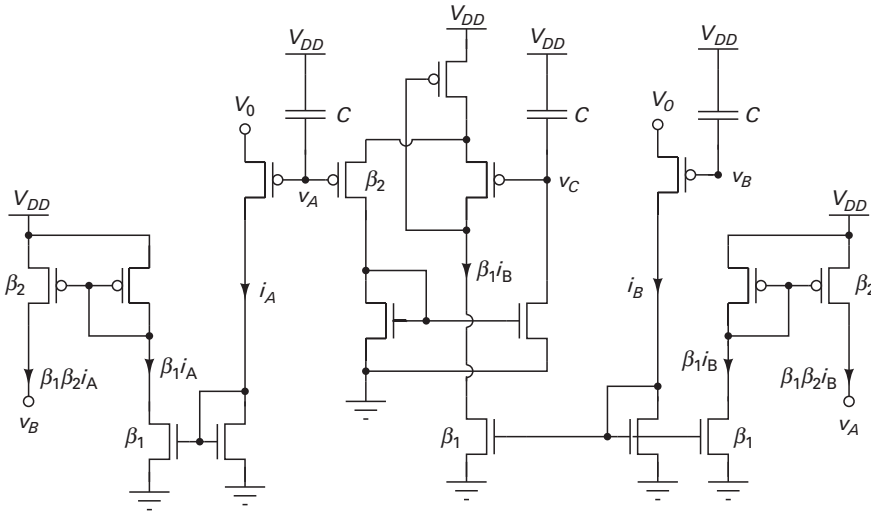


Figure 24.4. Second-order log-domain chemical reaction circuit. Reprinted with permission from [9] (©2009 IEEE).

forward-reaction current source (that exhibits Poisson noise statistics) hooked to a conductance proportional to K_d , which is in parallel with a capacitance (and the current source). The voltage on the capacitance represents the concentration of C . Due to the reverse-reaction current flowing through it, the conductance proportional to K_d exhibits Poisson statistics as well. In effect, we have a parallel RC circuit fed by a current source with shot noise from the current source and shot noise from the current flowing through the R . Note that the power spectral density of the current through R is NOT $4kTG$ but $2qI$ in such chemical resistances as we discussed when we derived Equation (24.7). If the forward-reaction current source has a value I , the voltage v_C will equilibrate at a value such that the backward-reaction current through R balances it. Thus, we may expect the noise voltage on the capacitor C to be given by

$$\begin{aligned} \overline{v_n^2} &= (2qI + 2qI)(R^2) \left(\frac{\pi}{2}\right) \left(\frac{1}{(2\pi)RC}\right) \\ &= \frac{q(IR)}{C} \end{aligned} \tag{24.18}$$

The signal-voltage power on the capacitor is given by

$$v_C^2 = (IR)^2 \tag{24.19}$$

Thus, the net SNR of the circuit in this scenario is given by

$$\begin{aligned} SNR &= \frac{v_C^2}{v_n^2} \\ &= \frac{C(IR)}{q} \end{aligned} \tag{24.20}$$

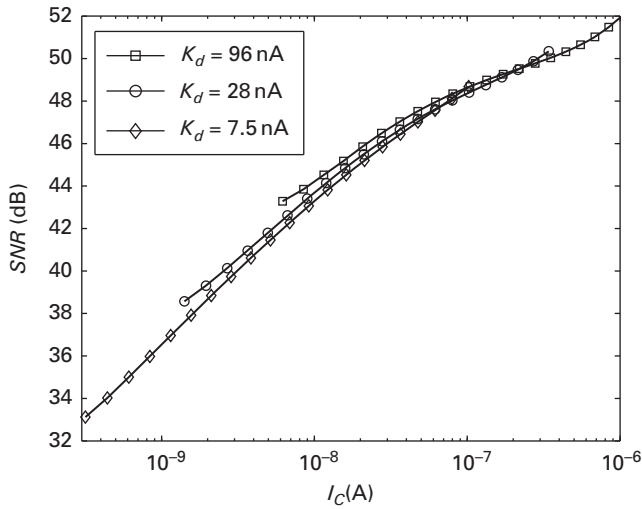


Figure 24.5. The SNR variation versus I_C when I_A and I_B are maintained constant in a bidirectional association reaction. Reprinted with permission from [9] (©2009 IEEE).

In the actual current-mode circuit, IR is represented by an equivalent output current I_C such that Equation (24.20) predicts that the SNR of the current-mode circuit increases as the mean value of I_C increases and is only dependent on the net value of I_C (or IR), not the value of R or K_d . Indeed, Figure 24.5 confirms these predictions when noise simulations are performed on the bidirectional current-mode equivalent circuit. Figure 24.5 indicates that the stochastics of the current-mode circuits that we have designed do indeed automatically represent those seen in chemical reactions. In Figure 24.5, the saturation at large SNR is primarily due to flicker noise. The value of C can be used to scale the SNR as was also confirmed by simulations (but not shown). At very low SNR (say below 20 dB) parasitic capacitances and leakage currents limit the reliable control of SNR in the circuit. In these situations, the circuit described in Figure 24.12 allows us to reliably add artificial noise in a quiet electronic circuit with the right Poisson properties. The circuit of Figure 24.12 is described later in the context of DNA-protein dynamics but it can be adapted for use in any chemical reaction.

A $1.5\text{ mm} \times 1.5\text{ mm}$ proof-of-concept protein-protein network chip with 81 second-order reaction blocks, 40 first-order reaction blocks, 40 zeroth-order reaction blocks, 32 state variables, 16 inputs and 8 outputs in a $0.18\text{ }\mu\text{m}$ process has been reported in [9]. The reaction rates, initial conditions, volume compartments of reactions (capacitances), and which molecular species are involved in which reaction are completely programmable via reconfigurable digital bits. The chip has the potential for fast highly parallel stimulation with stochastics and cell-to-cell variability automatically included. Data from this chip for a simple reaction network given by $A + A \rightarrow B$; $B \rightarrow C$ is shown in Figure 24.6 and compared with a MATLAB simulation of the same system. In both cases, we

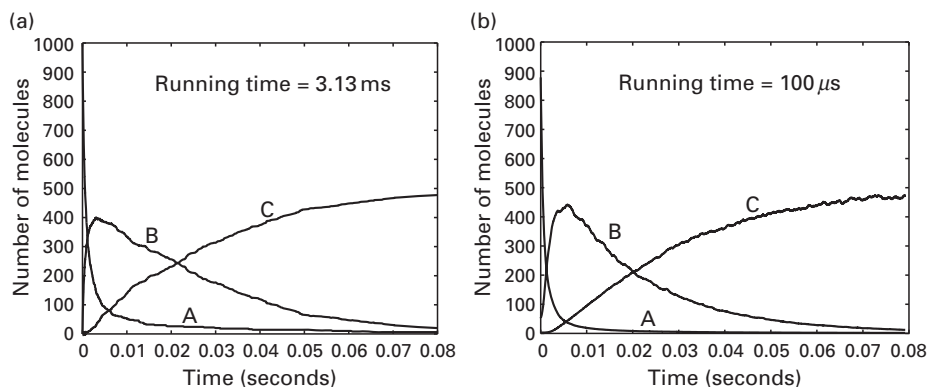


Figure 24.6a, b. MATLAB (a) versus chip data (b). Reprinted with permission from [9] (©2009 IEEE).

see that as A is consumed, B rises, and then as B is consumed and transformed to C, B falls, while C rises. The MATLAB simulation runs in 3.13 ms while the chip's simulation runs in 100 μ s. The performance speedup of 30 times in this first-iteration chip was limited by data-acquisition hardware not being able to acquire data from the chip fast enough. Due to the fast highly parallel nature of the analog implementations, speedups of 10^3 times should be possible in the near future and speedups greater than 10^6 times should eventually be possible.

The automatic inclusion of stochastics in the analog chips that we have described is highly beneficial for simulating large-scale protein networks in the cell in an ultra-fast fashion. In spite of efficient stochastic algorithms being available [10], the computation time of molecular-dynamics simulators increases precipitously when stochastics are included. Currently, the real-time simulation of just 30 state variables with stochastics is quite challenging. However, large-scale protein networks in the cell can have up to 30,000 state variables in human cells. Our knowledge of the topology and parameters of such biochemical networks is growing every day although our ability to predict what they will do, given this knowledge, is still very limited. Thus, programmable analog chips that rapidly emulate stochastic biochemical reaction networks in cells may be very important in the future in understanding and simulating cellular function on a large scale. The parallel and compact nature of the implementation allows scalability of large-scale networks onto a single chip or a few chips. Furthermore, they can be used to provide plausible ranges for unknown parameters in reaction networks via rapid exploration of such networks subject to certain known experimental facts and constraints. Elegant stimulus-design criteria for distinguishing between models for biochemical reaction mechanisms based on control theory can be used with such chips in the feedback loop [11]. Machine-learning techniques such as stochastic gradient descent, regression, and gradient descent can be implemented on a digital computer to measure and configure analog protein-network chips such that they optimize fits to experimental data, are consistent with known constraints, and/or

maximize objective functions known to be of biological importance like cell growth. In essence, analog chips that model chemical reaction networks can serve as ‘special-purpose’ ALUs that implement nonlinear dynamical systems optimized for simulating biochemical reaction networks.

24.3 Analog circuit models of gene-protein dynamics

Figure 24.7 illustrates the basics of gene-protein interactions in cells. An *inducer* molecule, e.g., glucose or S_X , may enter a cell and cause biochemical reaction events that eventually, e.g., via a protein-protein network, lead to the activation of a particular protein called a *transcription factor* X . When activated, $X \rightarrow X^*$, with X^* being the active form of the transcription factor. The activation of the transcription factor most often occurs because a molecule, typically the inducer, binds to the transcription factor and changes its shape. The activated transcription factor X^* can then bind to DNA near or within specific *promoter* binding sites on the DNA that have a particular sequence of A, T, C, or G nucleotides within them. These sites are effective in binding the particular transcription factor. *Transcription* is the process whereby the enzyme RNA polymerase (RNAP in Figure 24.7) converts the DNA sequence of a gene into a corresponding messenger RNA (mRNA) transcript sequence that is eventually translated into a protein. The binding of the transcription factor causes the transcription rate of a gene near the promoter to be increased if the transcription factor is an *activator* or decreased if the transcription factor is a *repressor*. In Figure 24.7, a repressor transcription factor Y that is activated to Y^* by an inducer S_Y is shown. Ribosome molecules in

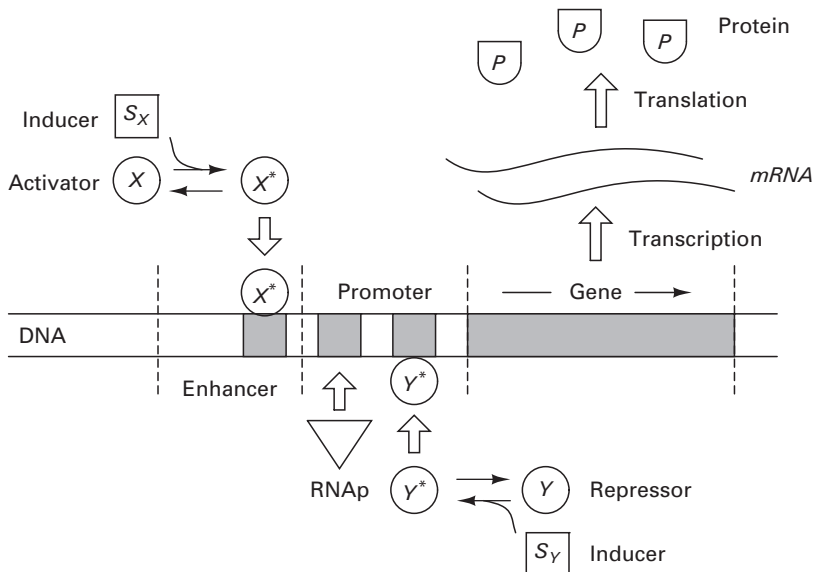


Figure 24.7. Basics of induction, transcription, and translation in cells.

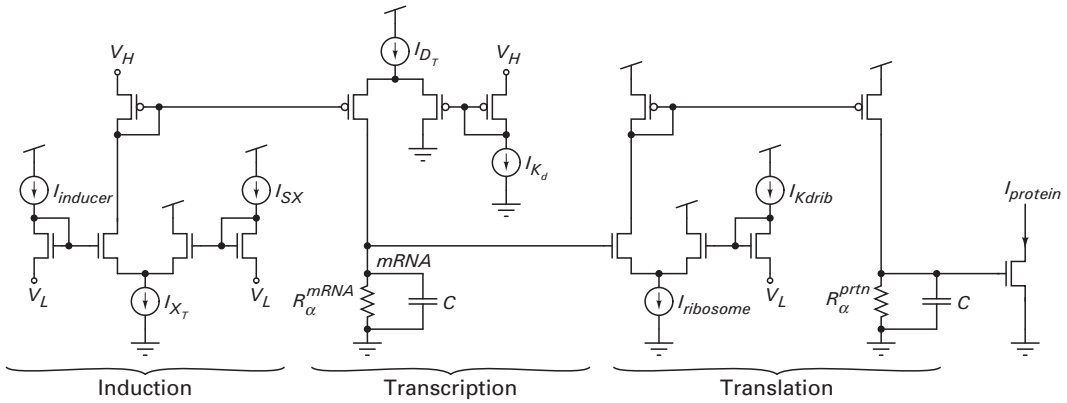


Figure 24.8. Basic induction, transcription, and translation circuit.

the cell *translate* the mRNA transcript into a sequence of corresponding amino acids to form a protein. The final translated protein can act as a transcription factor for other genes in a gene-protein network or affect other proteins in a protein-protein network or both. The translated protein can also serve as an activator or repressor for its own gene. Readers interested in further details of molecular biology should consult [1].

Figure 24.8 reveals a circuit model of induction, transcription, and translation. If the inducer concentration, $I_{inducer}$, is significantly greater than I_{SX} , the K_d for inducer-transcription-factor binding, most of the transcription-factor molecules X will be transformed into an active state X^* . The current output of the subthreshold differential pair that represents induction quantitatively models this process:

$$I_{X^*} = I_{X_T} \left(\frac{\frac{I_{inducer}}{I_{SX}}}{\frac{I_{inducer}}{I_{SX}} + 1} \right) \quad (24.21)$$

Equation (24.21) is an exact model of Michaelis-Menten binding as per Equation (24.3) with I_{X_T} representing the total concentration of transcription factor, X_T , whether activated or not. Similarly, if the activated transcription-factor concentration I_{X^*} is significantly greater than K_d , the dissociation constant for DNA-transcription-factor binding, the rate of production of mRNA transcripts by the enzyme RNA polymerase will be near its maximal value, assuming, without loss of generality, that the transcription factor in question is an activator. The current output, I_m , of the subthreshold differential pair that represents transcription in Figure 24.8 quantitatively models this process:

$$I_m = I_{D_T} \left(\frac{\frac{I_{X^*}}{I_{K_d}}}{\frac{I_{X^*}}{I_{K_d}} + 1} \right) \quad (24.22)$$

In Equation (24.22), I_m represents the rate of mRNA production and I_{D_T} is the maximal rate of mRNA production. Equation (24.22) suggests that the absence of activator shuts off mRNA production to 0. In practice, one can add a constant-current term to Equation (24.22) to model the fact that there is a basal mRNA production rate even when there is no activator present. Equation (24.22) can be converted into a repressor equation if we use current from the other arm of the transcription differential-pair in Figure 24.8. The current I_m leads to a final mRNA concentration described by a Laplace-transform lowpass filter equation

$$M_{RNA}(s) = I_m(s) \frac{R_\alpha^{mRNA}}{1 + R_\alpha^{mRNA} C s} \quad (24.23)$$

In Figure 24.8 and Equation (24.23), $mRNA \cdot R_\alpha^{mRNA}$ is the rate of degradation of mRNA due to enzymes that actively degrade mRNA in a linear fashion and C is the volume of the reaction compartment of the cell. The time course of transcription is typically determined by the $R_\alpha^{mRNA} C$ time constant since inducer binding is relatively rapid. Although Figure 24.8 represents mRNA as a voltage variable for simplicity, the $R_\alpha^{mRNA} C$ circuit can be replaced by a current-input current-output lowpass filter that outputs an I_{mRNA} current instead of an mRNA output voltage. If I_{mRNA} represents the mRNA concentration, we can represent the process of translation by the overall equation

$$I_{protein}(s) = I_{ribosome} \left(\frac{\frac{I_{mRNA}}{I_{Kdrib}}}{\frac{I_{mRNA}}{I_{Kdrib}} + 1} \right) \left(\frac{R_\alpha^{prtn}}{1 + R_\alpha^{prtn} C s} \right) \quad (24.24)$$

with parameters as shown in Figure 24.8. Typically, the protein degradation time constant $R_\alpha^{prtn} C$ is the largest time constant in the overall process, with a value ranging from 30 minutes (in bacteria in high-growth medium) to over 20 hours (in human cells). Certain proteins, for example, those in certain cells in the eye, may not be degraded at all.

Equations (24.21) through (24.24) represent the basics of gene-protein dynamics when chemical binding occurs between two molecules that are each monomers. Frequently, the transcription factor has maximal binding efficacy to DNA when it is a dimer (two identical molecules bound to each other) or is even a quadrimer (four identical molecules bound to each other). In such situations, Equation (24.22) can be well approximated by an equation of the form

$$I_m = I_{D_T} \left(\frac{\left(\frac{I_{X^*}}{I_{Kd}} \right)^n}{\left(\frac{I_{X^*}}{I_{Kd}} \right)^n + 1} \right) \quad (24.25)$$

where $n = 2$ in the case of dimer binding or 4 in the case of quadrimer binding [5]. The parameter n is often termed the ‘Hill coefficient’ and is implicitly 1 in Equations (24.21) through (24.24). At Hill coefficients that are large, Equation (24.25) is often

described by a digital approximation: if the transcription factor is an activator, we assume that mRNA transcript production is at its maximal rate I_{D_T} when $I_{X^*} > K_d$ and 0 otherwise; if the transcription factor is a repressor, we assume that mRNA transcript production is at 0 when $I_{X^*} > K_d$ and I_{D_T} otherwise.

Circuits to create Hill coefficients with any analog value from, say, 1 to 4 can be designed by exploiting a strategy similar to that used in Chapter 19 to create power-law coefficients in AGC circuits. The input diode-connected transistors in the differential pairs of Figure 24.8 are replaced by a transistor with a buffered WLR (Chapter 12) of transconductance G_1 from its drain to gate and a buffered WLR of transconductance G_2 from its gate to a reference. Programming of G_1 and G_2 with DAC currents then ensures that a power-law of approximately $(G_1 + G_2)/G_1$ is obtained.

Note that, for simplicity, we have ignored the body effect in Figure 24.8 by setting $\kappa = 1$. In an actual implementation, as we have discussed in Chapter 14 on current-mode circuits, source-tied-to-well pFET transistors should be used to implement all differential pairs and lowpass filters in Figure 24.8. In processes where the body of nFETs is fixed at a global substrate voltage, nFETs should only be used in fixed-ratio current mirrors.

24.4 Logic-like operations in gene-protein circuits

When *E. coli* are cultured in a medium that lacks glucose but has lactose, these bacteria increase the transcription rate of certain genes, which are normally expressed at a very low level. These genes produce proteins that help metabolize lactose to obtain energy, help transport lactose into the cell, and help detoxify toxic metabolites caused by lactose metabolism. If glucose is present, these genes are not expressed: it is significantly cheaper for the cell to metabolize glucose rather than lactose if glucose is present. Therefore, the bacteria do not bother making proteins useful for lactose metabolism if glucose is present. Effectively, the cell behaves as though the expression of these genes is based on the logical expression NOT (Glucose) AND Lactose.

Experiments have shown that the absence of glucose induces an activator transcription factor called CRP to become active and bind DNA in a certain enhancer region of the DNA. Thus, in Figure 24.7, activated CRP would correspond to X^* . The binding of CRP enhances the transcription rate of RNA polymerase in a catalytic fashion by helping recruit RNA polymerase to bind near the enhancer and thus begin transcription of genes near the enhancer region. The presence of lactose induces a repressor transcription factor called LacI to become inactive and unbind from DNA in a promoter region of the DNA that is adjacent to the enhancer region where CRP binds. Thus, in Figure 24.7, activated LacI would correspond to Y^* , and the inactivation of Y^* to Y by the lactose inducer would correspond to LacI unbinding from the DNA. RNA polymerase must bind to DNA in the promoter region for transcription of nearby genes to begin. The unbinding of LacI serves to unblock the binding of RNA polymerase on the promoter and consequently enables transcription to proceed. Thus, the interactions between the transcription factors on DNA is

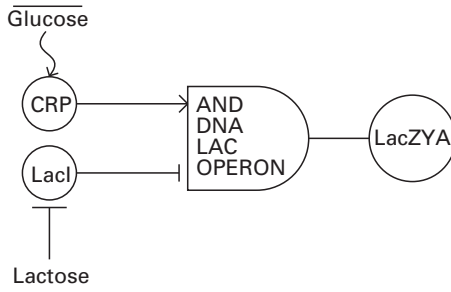


Figure 24.9. LacZ circuit. Reprinted with permission from [14] (©2009 IEEE).

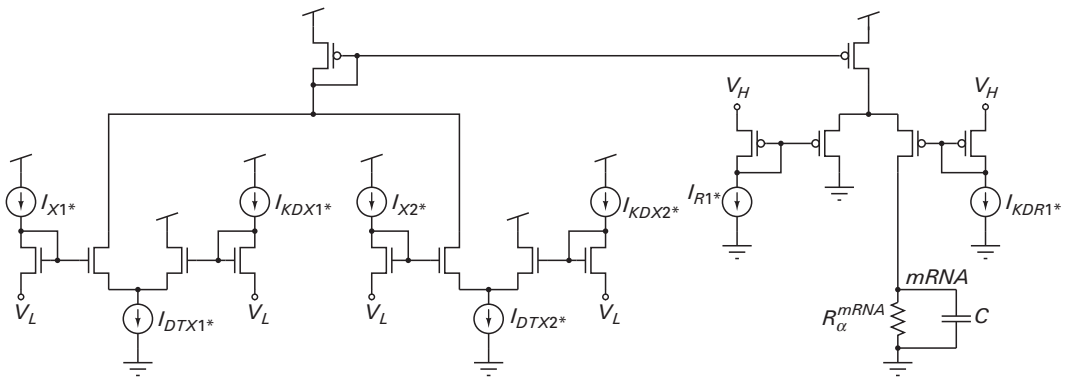


Figure 24.10. DNA analog logic circuit for $(X_1^* + X_2^*) \cdot \overline{R_1^*}$.

analogous to the manner in which multiple inputs affect the output of a logic gate as shown in Figure 24.9. The AND DNA Lac operon increases the transcription of the sequentially adjacent LacZ, LacY, and LacA genes, if the CRP activator is bound and the LacI repressor is unbound. These sequentially adjacent genes are said to be on a common *operon* whose transcription is controlled by the binding/unbinding of the CRP and LacI transcription factors to the enhancer and promoter DNA regions respectively, which are both near each other and near the Lac genes. In general, interactions between transcription factors can lead to multiple-input logic functions. The true interactions are, of course, not digital, but analog. Further details can be found in [12].

Figure 24.10 shows an example of an analog logic circuit that implements the function

$$M_{mRNA}(s) = \left(I_{DTX1}^* \left(\frac{\frac{I_{X1}^*}{I_{KDX1}^*}}{\frac{I_{X1}^*}{I_{KDX1}^*} + 1} \right) + I_{DTX2}^* \left(\frac{\frac{I_{X2}^*}{I_{KDX2}^*}}{\frac{I_{X2}^*}{I_{KDX2}^*} + 1} \right) \right) \left(\frac{1}{1 + \frac{I_{R1}^*}{I_{KDR1}^*}} \right) \left(\frac{R_{\alpha}^{mRNA}}{1 + R_{\alpha}^{mRNA} C s} \right) \quad (24.26)$$

This function is the analog version of the digital logic function $(X_1^* + X_2^*) \cdot \overline{R_1^*}$ and models the effect of two activator transcription factors X_1^* and X_2^* that

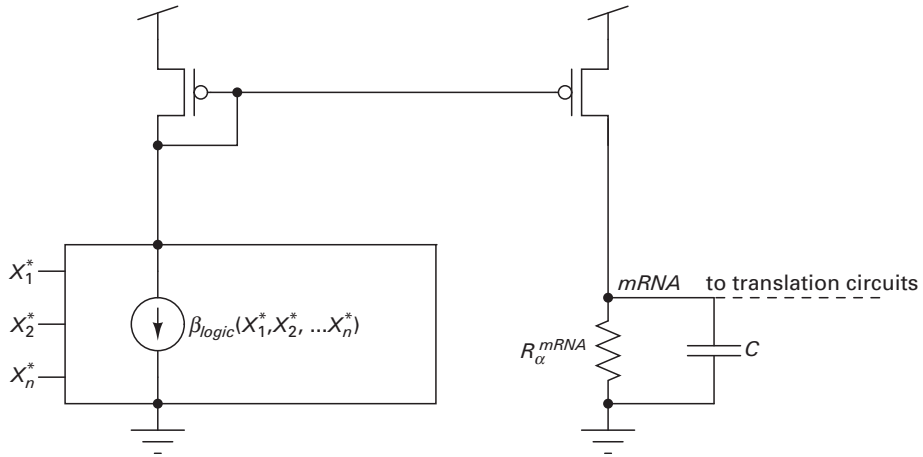


Figure 24.11. Simplified DNA logic circuit.

interact in an OR fashion and share a common repressor R_1^* . Equation (24.26) is a consequence of applying subthreshold differential-pair equations to each of the three differential pairs of Figure 24.10. These differential pairs model classic monomer Michaelis-Menten binding.

Figure 24.11 shows a hybrid analog-digital circuit that approximates gene-protein interactions with digital logic functions rather than with graded analog current-mode circuits as in Equation (24.26) or in Figure 24.10. In this circuit, the rate of production of mRNA varies with the value of a digital vector input D_n defined by

$$u(x) = 1 \text{ iff } x > 0 \text{ and } 0 \text{ otherwise}$$

$$D_n = \left(u\left(\frac{X_1^*}{K_{DX_1^*}} - 1\right), u\left(\frac{X_2^*}{K_{DX_2^*}} - 1\right), \dots, u\left(\frac{X_n^*}{K_{DX_n^*}} - 1\right) \right) \quad (24.27)$$

with the rate being a function of D_n given by

$$\beta_{mRNA} = \beta_{\text{logic}}(D_n) \quad (24.28)$$

That is for every discrete value of D_n , e.g., 001010, there is a corresponding analog rate of mRNA production, β_{001010} that can be listed in a lookup table. In essence, we have a logic DAC that converts D_n to analog production rates rather than a number-based DAC.

The presence of R^{mRNA} in Figure 24.11 models mRNA degradation. Translation circuits are implemented as shown in Figure 24.8 and only indicated with dotted lines in Figure 24.11. While Figure 24.11 is an approximate representation of DNA-protein interactions, and a decent approximation only at high Hill coefficients, it can still provide insight in several cases. In fact, an insightful systems-biology text is largely based on differential equations that are identical to those created by the circuit of Figure 24.11 [5].

24.5 Stochastics in DNA-protein circuits

Poisson noise in mRNA-production flux can be mimicked by Poisson electronic current noise in a manner analogous to that discussed previously for protein-production flux. However, the noise levels in mRNA production for some genes can be high enough such that extremely low currents and extremely small capacitances become necessary in electronics to mimic the same low signal-to-noise ratio (SNR) in biology. The resultant noise in electronics is then not well controlled or predictable. Therefore, it is sometimes advantageous to artificially introduce a controlled level of noise in a relatively quiet electronic circuit to mimic high-noise signals in biology. Figure 24.12 illustrates a circuit for doing so.

In Figure 24.12, the current-mode integrator with output capacitor C and I_{Rz} implement a current-mode version of the $R^{mRNA}C$ lowpass filter in Figure 24.11. That is, $2I_{Rz}$ and C correspond to I_A and C in Figure 14.9 in Chapter 14 on current-mode circuits. Similarly, v_{mRNA} and i_{mRNA} correspond to v_{OUT} and i_{OUT} in Figure 14.9 respectively. Instead of a constant $2I_{Rz}$ in a traditional current-mode lowpass filter, however, the leak current $2I_{Rz}$ is pseudo-randomly switched on and off with a duty cycle of 0.5. Thus, the average value of the leak current that sets the lowpass filter time constant is I_{Rz} as in a traditional circuit but the random switching introduces a stochasticity in this leak current. The log voltage on the current-mode capacitor is exponentiated and converted to a current i_{mRNA} that encodes the level of mRNA as in any current-mode circuit. The current i_{mRNA} is gained up by β_{SNR} and used to control the frequency, f_{CCO} , of a current-controlled oscillator (CCO). The output switching frequency of the oscillator is proportional to i_{mRNA} according to $f_{CCO} = \beta_{SNR} i_{mRNA} / q_{CCO}$, where q_{CCO} depends on design parameters internal to the CCO. Thus, as mRNA levels rise, the control current and switching frequency of the CCO rise in proportion. The linear feedback shift register (LFSR) converts the digital output of the CCO to a random switching signal via a classic pseudo-random-number generator technique [13]. Thus, the output of the LFSR randomly switches the I_{Rz} current on and off with a switching frequency f_{CCO} that is proportional to the mRNA level encoded by i_{mRNA} . Consequently, as mRNA levels rise, a consequence of a higher mRNA production rate, the arrival

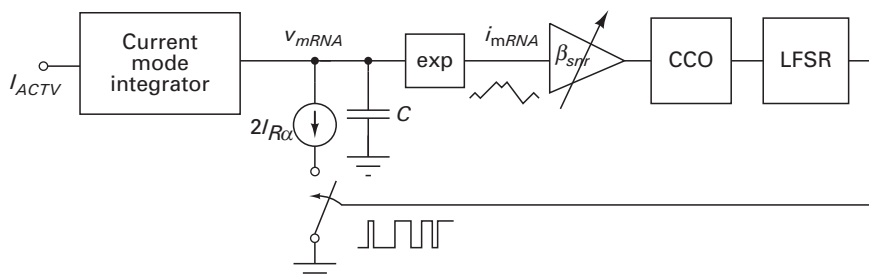


Figure 24.12. Artificial noise generation circuit for low SNR. Reprinted with permission from [14] (© 2009 IEEE).

rate, f_{CCO} , of charge packets with value $2I_{Rz}/f_{CCO}$ increases even though the mean value of current stays at $0.5f_{CCO}(2I_{Rz}/f_{CCO}) = I_{Rz}$. The noise power spectral density of the switching current at the log-voltage node is given by the usual shot-noise formula with an effective $q = I_{Rz}/f_{CCO}$ and the mean current equals I_{Rz} (see Chapters 7 and 8):

$$\Delta I_{psd}^2 = 2 \left(\frac{I_{Rz}}{f_{CCO}} \right) (I_{Rz}) \quad (24.29)$$

If the conductance at this node is $G(f)$, the output noise power spectral density is given by

$$\begin{aligned} \Delta I_{psdout}^2(f) &= 2 \left(\frac{I_{Rz}}{f_{CCO}} \right) (I_{Rz}) \frac{g_m^2}{G(f)^2} \\ &= 2 \left(\frac{I_{Rz}}{(\beta_{SNR} I_{mRNA} / q_{CCO})} \right) (I_{Rz}) \frac{I_{mRNA}^2 / (\phi_t / \kappa)^2}{G(f)^2} \\ &= 2 \frac{q_{CCO}}{\beta_{SNR}} \frac{(I_{Rz})^2}{G(f)^2 (\phi_t / \kappa)^2} I_{mRNA} \end{aligned} \quad (24.30)$$

while the output signal power is given by

$$I_{out}^2 = \frac{(I_{Rz})^2}{G(f)^2} \frac{I_{mRNA}^2}{(\phi_t / \kappa)^2} \quad (24.31)$$

since the dc input from the current mode integrator must be I_{Rz} as well. Comparing Equations (24.30) and (24.31), we see that the ratio of the output signal power and output noise power spectral density behave exactly as one would expect for a classic Poisson shot-noise current source except that the charge on the electron has been replaced by q_{CCO}/β_{SNR} . Thus, the value of q_{CCO}/β_{SNR} serves effectively like the charge on the electron, which we can increase if we want more noise (by decreasing β_{SNR}) and which we can decrease if we want less noise (by increasing β_{SNR}).

The input labeled I_{ACTV} in Figure 24.12 is a logical signal that is activated when a switching transition in D_n leads to mRNA production. The current I_{ACTV} represents $\beta_{logic}(D_n)$ in Equation (24.28). Transients in I_{ACTV} will lead to $R^{mRNA}C$ -like dynamics in the mRNA level. As mRNA levels change, the output noise of the circuit of Figure 24.12 will change as well ensuring that noise dynamics and signal dynamics are correlated as in any real biological or artificial system.

Figure 24.13 shows experimental data obtained from a chip containing this circuit. Relatively low values of SNR are set and measured. Note that the SNR is not in dB but in regular squared units. The protein SNR is higher than the mRNA SNR because translation of mRNA to protein involves additional lowpass filtering on the mRNA output (see Figure 24.8). The additional lowpass filtering reduces the output protein noise and improves SNR. Other measurements from the chip confirm that the probability distributions of currents are Poisson [14] as they should be.

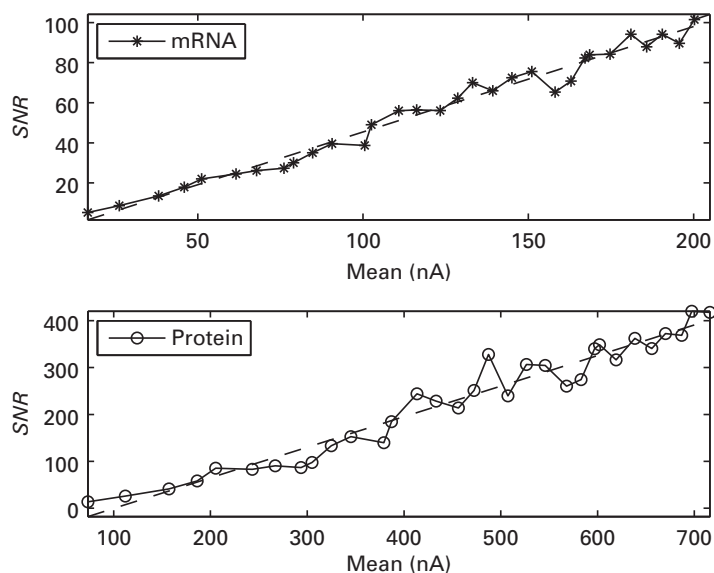


Figure 24.13. SNR measurements from the circuit of Figure 24.12. Reprinted with permission from [14] (©2009 IEEE).

24.6 An example of a simple DNA-protein circuit

Figure 24.14 shows an example feed-forward logic (FFL) circuit that is extremely common in *E. coli* bacteria and that has been extensively studied [5]. When the output genes of the circuit are activated, they produce proteins that are useful for metabolizing and processing arabinose, a sugar. The lactose circuit of Figure 24.9 implements NOT (glucose) AND lactose while the circuit of Figure 24.14 implements NOT (glucose) AND (arabinose). Hence, the circuits of Figures 24.9 and 24.14 have similar functions but there are significant differences in their topologies that lead to differences in how they process their inputs.

The CRP and AraC transcription factors that are activated by glucose and arabinose signals respectively, are in series in Figure 24.14. That is, AraC production begins only if the CRP protein, which is activated by the absence of glucose, activates transcription of genes that produce AraC. If arabinose is present, it induces AraC to become activated, and the combination of an active CRP and an active AraC lead to production of the AraBAD proteins via the AND DNA Ara operon. The logic of Figure 24.14 is redundant: it implements an AND function via the series combination of CRP and AraC and also via the AND DNA operon. In contrast, the logic of Figure 24.9 implements the AND function only via the AND DNA operon. Why does nature have such redundancy? Data in Figures 24.15 (a) and 24.15 (b) from an integrated-circuit chip that models the gene-protein circuit of Figure 24.14 illustrate the purpose of the redundancy. The data are in accord with work described in [5]. In this data, the arabinose inducer

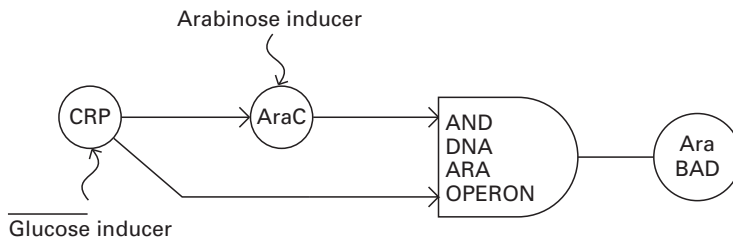


Figure 24.14. The arabinose circuit. Reprinted with permission from [14] (©2009 IEEE).

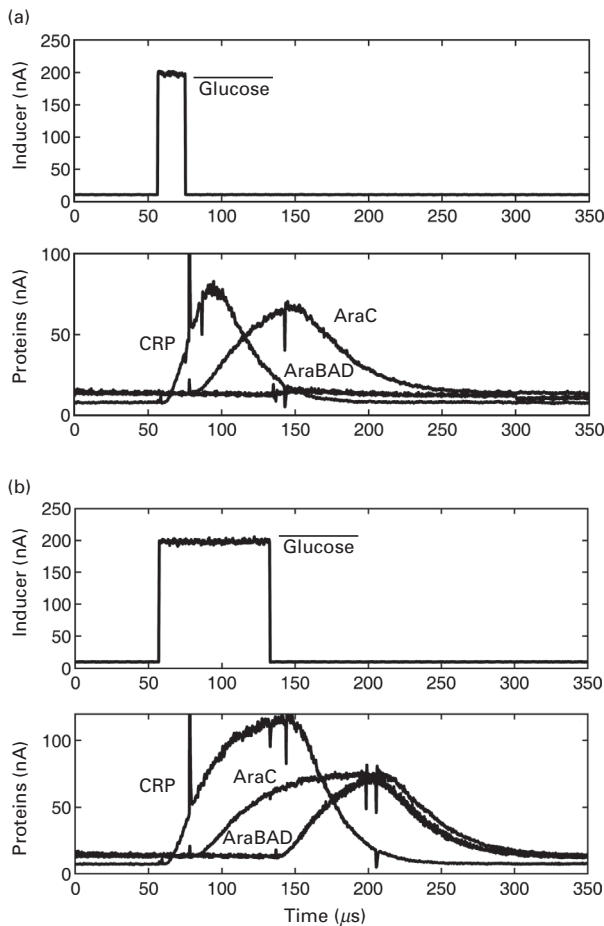


Figure 24.15a, b. Arabinose circuit responses for short (a) and long (b) pulse inputs of the inducer. The glitches are due to computer data-acquisition artifacts. Reprinted with permission from [14] (©2009 IEEE).

sugar concentration is large and constant such that AraC is instantly converted into its active form when produced. Figure 24.15 (a) shows that short absences of glucose inducer do not allow enough time for AraC protein production to build up and reach equilibrium such that sufficiently large amounts of active CRP and

AraC are not simultaneously present; thus, AraBAD protein production is never triggered if glucose is only briefly absent. Figure 24.15 (b) shows that long absences of glucose inducer allow enough time for AraC protein production to build up and reach equilibrium such that sufficiently large amounts of active CRP and AraC are simultaneously present; thus, AraBAD protein production is triggered if glucose is absent for a consistently long duration. Hence, the FFL circuit of Figure 24.14 ensures that the relatively expensive production of proteins needed to process arabinose, a sugar that has a higher cost/benefit ratio than glucose, is only initiated if glucose has been absent for a sufficiently long time.

In many molecular circuits in bacteria and yeast, delays in transcription and translation are relatively negligible compared to mRNA or protein degradation time constants, respectively. Thus, they can often be approximated by increasing these time constants a little. In mammalian cells, however, the delay in the transcription of relatively long genes, which is ~ 30 minutes, can exceed the mRNA degradation time, which can range from 10 minutes to 10 hours. In certain feedback circuits, the representation of these delays is crucial. Such delays can be programmably represented by conventional clock-counting or one-shot techniques that activate β_{logic} in Figure 24.11 only after a delay. Such delays can be programmably incorporated into the chip from which the data of Figures 24.13 and 24.15 were gathered as described in [14].

24.7 Circuits-and-feedback techniques for systems and synthetic biology

Circuits can often shed insight into biology that is harder to obtain in a different language. For example, work described in [15] has shown how slow outer hair cells in the ear with a time constant of 1 ms can amplify sounds at frequencies over 100 kHz, a two-decade-old mystery. This work shows that while the open-loop time constant of the piezoelectric outer hair cell is 1 ms, the presence of negative feedback in the cochlea with a gain-bandwidth product that is large enough results in a closed-loop system capable of amplification at higher frequencies: the process is analogous to how an operational amplifier with an open-loop time constant of 10 Hz can exploit negative feedback to build an amplifier with a gain of 10^3 at 10 kHz because its gain-bandwidth product is 10^6 . In the cochlea, the situation is slightly more complex since the overall negative-feedback loop in the cochlea has a resonance as well, but a simple negative-feedback and root-locus analysis shows that the resonant gain is also improved by negative feedback, thus further enabling high-frequency amplification [15]. Thus, circuits-and-feedback concepts can shed light into how biological systems work. This book has presented circuit models of the heart in Chapter 20, of the neuron in Chapter 15, and of the ear, vocal tract, retina, and neurons in Chapter 23, which allow us to rapidly understand how these systems work. Circuit models are efficient because they are inherently designed to graphically represent interactions between devices in a system in a meaningful way that lead to functional sub-blocks. Such sub-blocks can parse complex systems

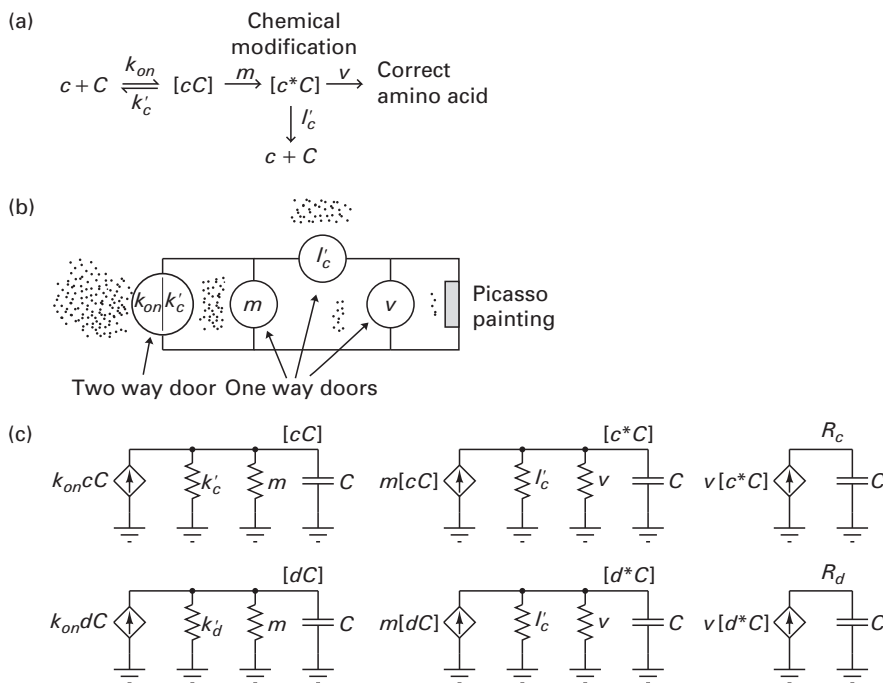


Figure 24.16a, b, c. (a) Kinetic proofreading. (b) Picasso-lover analogy. (c) Circuit analogy.

into meaningful network motifs such as the FFL sub-block that we have discussed [5]. In contrast, representing complex systems via a set of random connections amongst network nodes does not yield much insight into the function of the complex system although it may be mathematically equivalent to a circuit.

As an example of how circuits can shed insight into systems biology, we illustrate how the language of circuits can provide a useful interpretation of kinetic proofreading circuits in cells, which are ubiquitously present in many of its subsystems. Kinetic proofreading allows the cell to reduce the discrimination error rate between highly similar molecules without spending too much time or designing highly specific recognition molecules to do so [16]. Figure 24.16 (a) illustrates the biochemical process; Figure 24.16 (b) provides a Picasso-lover analogy of the process that is adapted from a textual description of this analogy in [5]; Figure 24.16 (c) provides a circuit model of the process.

Figure 24.16 (a) illustrates the chemical-reaction cascade involved in the binding of a specific tRNA codon molecule, which contains a three-letter snippet of RNA, to a complementary three-letter snippet in an mRNA transcript to create a bound species. The tRNA codon is denoted by c , the corresponding mRNA snippet is denoted by C , and the bound species is denoted by cC . Such binding triggers events within the ribosome protein translating machinery in the cell. These events translate a three-letter codon word formed from an alphabet of 4 molecular letters to a particular amino acid. Each of the 64 possible codons is translated by the

ribosome machinery to a corresponding amino acid that it codes for. Some amino acids are coded for by more than one codon such that there is some redundancy in the many-to-one translation mapping. The net result is that the ribosome machinery translates the sequence of letters in mRNA to an equivalent sequence of amino acids. Certain codons are not translated into amino acids but function as ‘start’ and ‘stop’ codons for the ribosome machinery. Further details are described in any standard molecular-biology text, e.g., [1].

To prevent a translation error, only the correct complementary tRNA codon must bind to the mRNA, such that a wrong amino acid is not incorporated into the protein. Since two tRNA codons that differ by only one letter have similar binding K_d 's, however, there is a relatively high probability of error ($\sim 10^{-2}$). One solution is to simply design the binding to be more specific, but this solution costs time: since the association rate, k_{on} , is diffusion-limited and similar for all tRNA codons, the specificity of binding is decided by k'_c , the rate of dissociation or unbinding. High specificity implies that each codon is bound for a long time because of a low dissociation rate k'_c . Since the ribosome can't move to translating the next codon until the current bound tRNA drops off the mRNA, a low k'_c improves specificity but lowers the overall rate of translation. Even with this undesirable tradeoff, designing highly specific binding with a low k'_c is not easy.

To reduce the error rate of translation, the cell implements the methylation scheme shown in Figure 24.16 (a). The bound tRNA species cC is methylated by enzymes at a rate m to create the species c^*C via a unidirectional reaction; only the methylated species leads to translation at a unidirectional rate v . The affinity of the methylated tRNA codon for the mRNA is similar to that of the unmethylated tRNA. Thus, the rate of dissociation l'_c of the methylated species from the mRNA is proportional to k'_c and high-affinity tRNA codons bind longer to the mRNA, whether methylated or unmethylated. Unlike the reversible binding of the k_c/k'_c process, however, if the tRNA codon unbinds from the mRNA, it dissociates into an un-methylated form and cannot mount back onto the mRNA directly until it reforms cC as shown in Figure 24.16 (a). High-affinity tRNA codons are more likely to remain bound through the process of methylation and not fall off the mRNA; wrong tRNA codons are more likely to fall off and have a significantly lower probability of translation in a given time: these tRNA codons need to ‘get back in line’ to the beginning of the chemical cascade, form cC , and then form c^*C to get translated, which delays their translation. The unidirectionality and delay of methylation thus serve to improve the probability of correct translation.

The Picasso-lover analogy of Figure 24.16 (b) is useful in understanding kinetic proofreading. In a particular museum of fine arts, we would like to separate true Picasso lovers from fake ones who are not as sincerely passionate about his paintings. Given their higher affinity for Picasso, true Picasso lovers are more likely to linger for a longer time near one of his paintings or wait longer to see it than fake lovers. The k_{on}/k'_c two-way door in Figure 24.16 (b) represents the rate at which Picasso lovers enter (k_{on}) and leave (k'_c) a cC chamber with higher-affinity lovers having a lower leaving rate k'_c . The one-way ‘ m ’ door allows those in the cC

chamber to enter the c^*C chamber at a rate m . Those who enter this chamber can leave it via the one-way l'_c door at a rate l'_c that is proportional to their k'_c . If they do so, because they've been too impatient to wait to see the Picasso painting, they need to get back in line and re-enter via the two way k_{on}/k'_c door to see the Picasso painting again. Thus, in the c^*C chamber, those with low k'_c and consequently low l'_c have a higher probability of being present than fake lovers who've gotten impatient and left. The one-way ' v ' door finally rewards those left in the c^*C chamber to enter the chamber where the Picasso painting is actually displayed at a rate v . Thus, only true Picasso lovers will likely see the painting and have their desire to see it translated into reality while others will likely have left since they had two chances to do so.

Figure 24.16 (c) is the circuit representation of Figures 24.16 (a) and 24.16 (b). The same identical circuit is shown for a tRNA codon c and a tRNA codon d with differing rates of unbinding in methylated and unmethylated states. The tRNA codon c represents a true codon while the tRNA codon d represents a codon that can falsely bind to the mRNA. We can see from this circuit immediately that the ratio of wrongly translated d , R_d , to correctly translated c , R_c , is given by simple analysis of a two-stage 'cascaded amplifier' topology:

$$\begin{aligned} \frac{R_d}{R_c} &= \frac{d}{c} \left(\frac{k'_c + m}{k'_d + m} \right) \left(\frac{l'_c + v}{l'_d + v} \right) \\ &\approx \frac{d}{c} \left(\frac{k'_c}{k'_d} \right) \left(\frac{l'_c}{l'_d} \right) \\ &= \frac{d}{c} \left(\frac{k'_c}{k'_d} \right)^2 \end{aligned} \quad (24.32)$$

where the approximation holds if $m \ll k'_c$ or k'_d and $v \ll l'_c$ or l'_d . Typically, c and d are equally abundant such that $d/c \approx 1$ in Equation (24.32). By having an additional stage of methylated amplification, we improve the R_d/R_c error rate from a linear dependence on k'_c/k'_d to a square dependence on k'_c/k'_d in Equation (24.32). Thus, if $k'_c/k'_d = 10^{-2}$ the mistranslation error rate is reduced to 10^{-4} because of the single methylation stage of amplification. If there are n stages of methylation, we improve the R_d/R_c ratio by an $(n + 1)$ th power law due to $(n + 1)$ gain stages of amplification. Thus, kinetic proofreading is seen to be analogous to improving the discriminability of one set of proportional resistances (the c set) from another set of proportional resistances (the d set) by having them be part of a multiple-gain-stage topology rather than a single-gain-stage topology. Since delays or time constants from multiple gain stages only add while gains multiply, kinetic proofreading exploits the energy-efficient principle of distributed-gain amplification, a principle common in photoreceptors [17], in the cochlea [18], in the dendrites of neurons, and in transmission-line circuits in general. Chapter 23 discusses several distributed-gain transmission-line topologies in some depth. Furthermore, amplification requires one-way propagation of signals to prevent loads in late stages of amplification from compromising performance in early stages. The unidirectionality of the methylation process ensures such one-way propagation.

Robustness-efficiency, analog-digital, and other feedback-circuits-and-systems tradeoffs occur in cells just as in ultra-low-power analog and mixed-signal circuit design. Ultra-low-power analog electronic circuits face very similar tradeoffs like cells in biology because of their need to operate quickly, accurately and robustly despite mismatched and noisy components and signals, a necessary consequence of having very low levels of available power and space. Thus, analog circuits can shed insight into cellular systems biology just as they have in systems neurobiology in the past [19], [20]. They can also lead to the creation of new synthetic-biology circuits that are borrowed from circuit design. Simple topologies like ring oscillators have already been created [21] but there is still a lot of room for the creation of interesting circuits in cells that may truly have important medical applications. For example, next-generation antibiotic design involves the clever use of genetic-circuit engineering with bacteriophages [22]. Cellular biology, in turn, which performs 10 million biochemical operations at 1 pW of power, can inspire new circuit and system designs as several neurobiological architectures in the ear, eye, and brain have previously done (see Chapter 23). It is the author's firm belief that the field of cytomorphic electronics that we have suggested in this chapter is a field waiting to be born. This chapter has just scratched its surface. We shall now briefly highlight two broad areas that we believe to be particularly promising for the future.

24.7.1 Circuits-and-feedback analysis of stochastics and system dynamics in a cell

In many chapters of this book, we have shown how a thorough analysis of the noise performance of an ultra-low-power circuit allows quantitative predictions of its stochastic performance that are confirmed by experiment (for example, see Chapters 8, 11, 12, 13, 15, and 19). We have shown how noise sources that occur at different points in a circuit or equivalently at different points in a feedback block diagram have differing noise transfer functions (for example, see Chapters 11, 12, 13, 14, 15, 19, and 20) that make their variability more or less important. The same process can be applied to cells. The classic two-stage transcription-translation process of a cell, along with activation of the transcription factor, and binding of the transcription factor to DNA, is shown in Figure 24.17 (a). The feedback block diagram of Figure 24.17 (b) represents a simplified version of Figure 24.17 (a) that represents typical cellular operation. The square wave A in Figure 24.17 (b) represents rapid binding (k_a) and unbinding (γ_a) of the transcription factor to DNA in Figure 24.17 (a), which typically occurs at a fast enough rate such that it can be represented by a mean bound \bar{A} in the lowpass circuits that follow it as in Figure 24.17 (c). Simplification of the block diagram of Figure 24.17 (b) and representation of the bound transcription factor concentration by its mean results in Figure 24.17 (c). Note that A is itself the result of a fast inducer binding-and-unbinding process to the transcription factor, which activates the transcription factor from X to X^* . The block diagram of Figure 24.17 (b) is also a simplified representation of the circuit of Figure 24.8.

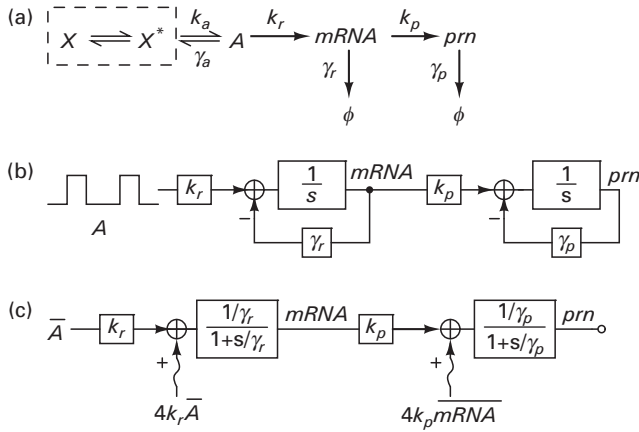


Figure 24.17a, b, c. (a) Induction, transcription and translation processes within a cell. (b) A feedback block diagram representation of Figure 24.16 (a). (c) Simplification of the feedback block diagram of Figure 24.16 (b). Reprinted with permission from [14] (©2009 IEEE).

The input shot-noise sources in Figure 24.17 (b) are due to transcription/translation molecular production (k) and degradation (γ) rates, which are balanced and equal to each other [14]. Analysis of Figure 24.17 (c) reveals that the total mRNA and protein power spectral densities are then given by

$$\begin{aligned}\sigma_{mRNA}^2 &= \frac{k_r \bar{A}}{\gamma_r} = \overline{mRNA} \\ \beta &= \frac{k_p}{\gamma_p} \\ \overline{prn} &= \beta \overline{mRNA} \\ \sigma_{prn}^2 &= \overline{prn} (\beta + 1)\end{aligned}\quad (24.33)$$

Equation (24.33) is a good model of the noise if the dynamics of protein degradation are much slower than that of mRNA degradation, i.e., $\gamma_p \ll \gamma_r$, such that the effective noise bandwidth is set by the protein degradation time constant, which is typically the case.

If we represent the mRNA concentration by the base current in a bipolar and the protein concentration by a collector current in a bipolar transistor, then Equation (24.33) exhibits the same mean and stochastic properties as the base and collector current in the bipolar:

$$\begin{aligned}\sigma_{base}^2 &= 2q\bar{i}_B(\Delta f) \\ \bar{i}_C &= \beta\bar{i}_B \\ \sigma_{coll}^2 &= 2q\bar{i}_C(\beta + 1)(\Delta f)\end{aligned}\quad (24.34)$$

The ‘burst factor’ β in Equation (24.33) is the protein/mRNA amplification ratio just like the current gain in bipolar transistors. Not surprisingly, there is

excess noise of $(1 + \beta)$ because the amplified base-current (mRNA) noise dominates over the intrinsic collector (protein) noise. Experimental measurements of noise in cells confirm Equation (24.33) exactly and use a full-blown stochastic analysis to derive it [23]. The simple circuits insight afforded by the similarity of Equations (24.34) and (24.33) makes the stochastic analysis transparent. Therefore, we can leverage off 50 years of knowledge in circuit design to shed insight into what biology is doing. The mathematical soul of an architecture can be very similar across different fields although its physical embodiment in each field appears to be very different. Therefore, the wheel is often reinvented in each field.

While biochemical circuits have quadratic nonlinearities due to association and dissociation reactions, making purely linear-systems analyses inadequate, one can still perform small-signal and stochastic analyses about equilibrium molecular concentrations in the cell that shed insight. Furthermore, large-signal analyses that are performed by holding one molecular concentration constant while varying that of another in an association or dissociation reaction are still useful (e.g. see the Michaelis-Menten resistive-divider analysis of Figure 24.2 in this chapter). Indeed, engineering analyses have been done in cells for small-scale systems and have lead to results in good accord with experiment [24]. In the future, techniques for noise analysis of circuits that have been expounded in this book could be ported over to analyze stochastics in cells on a larger scale than the basic Equation (24.33). Stochastic variation of protein concentrations within cells is highly significant and important for predicting a cell's response to its environment or to drug treatments. For example, a recent paper has shown that variations in protein concentration successfully account for variability in the response of tumor cells to chemotherapy treatment for cancer [2].

24.7.2 Return-ratio robustness analysis of parameter-and-topology variations in a cell

In Chapter 10, we showed how return-ratio techniques allow us to predict the variation in the closed-loop transfer function of a circuit when one of its parameters varies. Specifically, we derived that the relative change in the transfer function of a circuit, $d(TF_{gm})/TF_{gm}$, is related to the relative variation in the parameters of one of its elements, dg_m/g_m , according to

$$\frac{d(TF_{gm})}{TF_{gm}} = \left(1 - \frac{TF_0}{TF_{gm}}\right) \left(\frac{dg_m/g_m}{1 + R_{inputunloaded}}\right) \quad (24.35)$$

where TF_0 is the transfer function when $g_m = 0$ and $R_{inputunloaded}$ is the return ratio of the element. From Figures 24.4, 24.8, 24.10, or 24.11, variations in gene or protein parameters can be mapped to equivalent variations in circuit parameters. Equation (24.35) can then be used to predict how robust the circuit is to variation in a particular circuit parameter. Such an analysis can then shed insight into which gene/protein mutations and alterations sensitively impact the performance of a network and which do not. Gene knockouts represent an extreme version of this

paradigm with g_m changed from a finite value to 0. Such analyses can be considerably more subtle and robust to model error than digital-circuit techniques that have attempted to do the same by treating all variations as ‘on’ or ‘off’ and modeled all DNA circuits as being purely digital.

24.8 Hybrid analog-digital computation in cells and neurons

Computation in a neuronal network and computation in a gene-protein network share intriguing similarities at the signal, circuit, and system level. Table 24.1 below highlights some of these similarities.

These analogies suggest that neuronal networks in the brain have similarities to ultra-fast, highly plastic, large-scale gene-protein networks with lots of connections per node. The speed of neuronal responses is matched to the time scales

Table 24.1 Similarities between neuronal and cellular computation

Property	Neuronal equivalent	Cellular equivalent
1. Basic computational unit device	A neuron	A gene
2. Discrete symbolic digital output of device	A spike	An mRNA transcript
3. Translation of symbol to signal	Post-synaptic potential (PSP)	Translation of mRNA transcript to protein
4. Processing of signals to create symbols	Analog and digital dendritic processing of multiple inputs to neuron	Analog logic circuits on DNA from multiple inputs
5. Connection weighting	Synaptic weight	K_d and transcription-factor binding
6. Kinds of connections	Excitatory and inhibitory	Activatory and repressory
7. Dale’s rule	Output connection signs of a single neuron are correlated	Output connection signs of a single gene are correlated
8. Topological similarities	Shunting inhibition near soma with many excitatory inputs at other dendritic locations	Common repressor on DNA promoter with many activator transcription factor inputs.
9. Adaptation	Learning	Evolution
10. Connections per node	~6000	~12
11. Number of nodes	~22 billion	~30,000
12. Distributed ZY transmission-line processing	In dendrites	Reaction-diffusion networks within and outside cells.
13. Power consumption	~0.66 nW per neuron 22 billion neurons in the brain	~1 pW per cell ~100 trillion cells in the body

at which the brain needs to control the body to react to fast changes in its environment. The speed of cellular responses is matched to the time scales at which the gene-protein network needs to control the cell to react to slow changes in its environment. Therefore, neuromorphic and cytomorphic circuits may share several similarities. In fact, the hybrid state machine (HSM) that was discussed in Chapter 22 (see Figure 22.9 (b)) and Chapter 23 on neuromorphic electronics functions as a useful description of computation within a cell as well: the analog state of the HSM is represented by protein concentrations and analog processing is accomplished via protein-protein interactions; the digital state of the HSM is represented by a subset of active/inactive genes; the configuration of these genes alters a binary control vector that affects protein production rates; protein concentrations that cross certain thresholds create logical comparator transitions (spikes are derivatives of these) that serve as inputs to the analog logic DNA gates (as opposed to a hard finite state machine in the HSM). Networks of cells can communicate and compute as networks of HSMs. Finally, we should mention that protein-protein biochemical networks perform computations that are similar to those of neuronal networks as well: similarities in pattern recognition in kinase protein networks and in *C. elegans* neuronal networks are discussed in [5].

The similarities between neuronal computation and cellular computation imply that the principles for energy-efficient operation that we discussed in Chapter 22 and that we showed are obeyed by neurobiology in Chapter 23 are also obeyed by the cell. In fact, since cells arose much earlier than brains in evolution, it may be more accurate to say that the cell is the pioneer of low-power biological computation. Neurons in the brain may have inherited many of the nice energy-efficient computational principles in the cell for free, and reapplied them on faster time scales and in networks with more connectivity and relatively fast plasticity.

In Chapter 23, we discussed ZY transmission lines in the context of neurobiological computation in dendrites, the cochlea, the retina, and vocal tract. Distributed ZY transmission lines are used in cells as well: ingenious ZY transmission lines with diffusion-based resistive Z and quadratic/polynomial shunt Y conductances implement spatially decaying molecular profiles [5]. These profiles are robust to variations in conditions at the beginning of the line: if the local concentration at a point on the line increases, the polynomially increasing Y causes a faster decay, restoring the profile to its invariant shape; if the local concentration at a point on the line decreases, the polynomially increasing Y causes a slower decay, once again restoring the profile to an invariant shape. The use of nonlinear negative feedback in the ZY transmission line to create invariant spatial profiles is analogous to the use of nonlinear negative feedback in the diode-capacitor circuit of Chapter 23 (see Figures 23.14 (a) and (b) and Equation (23.35)). There, we described how to create invariant temporal profiles that are robust to initial conditions on the capacitor through the use of an exponential nonlinearity (an infinitely high-order polynomial); here we create invariant spatial profiles that are robust to conditions at the beginning of the line.

Such ZY transmission lines are exploited by cells during development to ensure robustness in morphogen gradients independent of variations in protein-production rates. The concentrations of morphogen molecules can decide the fate of a cell during development, morphing it from being a universal stem cell (say) to a neuron depending on the concentration of the morphogen. Therefore, the robust self-assembly of a human being is in part determined by ingenious analog non-linear partial differential equations within our mothers! As the Nobel Prize winning physicist, Richard Feynman, said: “The imagination of nature is far, far greater than the imagination of man” [25].

References

- [1] Harvey F. Lodish. *Molecular Cell Biology*, 6th ed. (New York: W.H. Freeman, 2008).
- [2] S. L. Spencer, S. Gaudet, J. G. Albeck, J. M. Burke and P. K. Sorger. Non-genetic origins of cell-to-cell variability in TRAIL-induced apoptosis. *Nature*, **459** (2009), 428–432.
- [3] K. A. Janes, J. G. Albeck, S. Gaudet, P. K. Sorger, D. A. Lauffenburger and M. B. Yaffe. A systems model of signaling identifies a molecular basis set for cytokine-induced apoptosis. *Science*, **310** (2005), 1646–1653.
- [4] Bernhard Palsson. *Systems Biology: Properties of Reconstructed Networks* (New York: Cambridge University Press, 2006).
- [5] Uri Alon. *An Introduction to Systems Biology: Design Principles of Biological Circuits* (Boca Raton, FL: Chapman & Hall/CRC, 2007).
- [6] D. Baker, G. Church, J. Collins, D. Endy, J. Jacobson, J. Keasling, P. Modrich, C. Smolke and R. Weiss. Engineering life: building a fab for biology. *Scientific American*, **294** (2006), 44–51.
- [7] Thomas Fischer Weiss. *Cellular Biophysics* (Cambridge, Mass.: MIT Press, 1996).
- [8] Gene F. Franklin, J. David Powell and Abbas Emami-Naeini. *Feedback Control of Dynamic Systems*, 5th ed. (Upper Saddle River, N.J.: Pearson Prentice Hall, 2006).
- [9] S. Mandal and R. Sarpeshkar, Log-domain Circuit Models of Chemical Reactions. *Proceedings of the IEEE Symposium on Circuits and Systems (ISCAS)*, Taipei, Taiwan, 2009.
- [10] D. T. Gillespie. A general method for numerically simulating the stochastic time evolution of coupled chemical reactions. *Journal of Computational Physics*, **22** (1976), 403–434.
- [11] J. F. Apgar, J. E. Toettcher, D. Endy, F. M. White and B. Tidor. Stimulus design for model selection and validation in cell signaling. *Public Library of Science Computational Biology*, **4** (2008), e30.
- [12] M. Ptashne and A. Gann. *Genes and Signals* (Cold Spring Harbour, New York: CSHL Press, 2002).
- [13] R. N. Mutagi. Pseudo noise sequences for engineers. *Electronics and Communication Engineering Journal*, **8** (1996), 79–87.
- [14] S. Mandal and R. Sarpeshkar. Circuit models of stochastic genetic networks. *Proceedings of the IEEE Biological Circuits and Systems Conference*, Beijing, China, 2009.

- [15] T. K. Lu, S. Zhak, P. Dallos and R. Sarpeshkar. Fast cochlear amplification with slow outer hair cells. *Hearing Research*, **214** (2006), 45–67.
- [16] J. J. Hopfield. Kinetic proofreading: a new mechanism for reducing errors in biosynthetic processes requiring high specificity. *Proceedings of the National Academy of Sciences*, **71** (1974), 4135–4139.
- [17] M. Tavakoli, L. Turicchia and R. Sarpeshkar. An ultra-low-power pulse oximeter implemented with an energy efficient transimpedance amplifier. *IEEE Transactions on Biomedical Circuits and Systems*, (2009).
- [18] R. Sarpeshkar, R. F. Lyon and C. A. Mead. A low-power wide-dynamic-range analog VLSI cochlea. *Analog Integrated Circuits and Signal Processing*, **16** (1998), 245–274.
- [19] Carver Mead. *Analog VLSI and Neural Systems* (Reading, Mass.: Addison-Wesley, 1989).
- [20] D. W. Tank and J. J. Hopfield. Collective computation in neuron like circuits. *Scientific American*, **257** (1987), 104–114.
- [21] M. B. Elowitz and S. Leibler. A synthetic oscillatory network of transcriptional regulators. *Nature*, **403** (2000), 335–338.
- [22] T. K. Lu and J. J. Collins. Engineered bacteriophage targeting gene networks as adjuvants for antibiotic therapy. *Proceedings of the National Academy of Sciences*, **106** (2009), 4629.
- [23] E. M. Ozbudak, M. Thattai, I. Kurtser, A. D. Grossman and A. van Oudenaarden. Regulation of noise in the expression of a single gene. *Nature Genetics*, **31** (2002), 69–73.
- [24] J. T. Mettetal, D. Muzzey, C. Gomez-Uribe and A. van Oudenaarden. The frequency dependence of osmo-adaptation in *Saccharomyces cerevisiae*. *Science*, **319** (2008), 482.
- [25] R. P. Feynman. *The Pleasure of Finding Things Out: The Best Short Works of Richard P. Feynman* (Cambridge, Mass.: Perseus Books, 1999).